Materials Advances

ROYAL SOCIETY OF CHEMISTRY

PAPER

View Article Online
View Journal

Cite this: DOI: 10.1039/d6ma00292g

DFT and AIMD predictions of Li_2XBH_6 (X = Li, Na, K) double perovskites for efficient hydrogen storage and photocatalytic applications

Partha Podder,[ab] Joy Kumar Sharkar,[ab] Md. Al-Amin,[ab] R. M. Tanvir,[ab] Siyam Sheikh,[ab] Md Tarikal Nasir,[cd] A. Rayhan[d] and S. Mahmud *[ab]

Received 3rd March 2026,
Accepted 21st April 2026

DOI: 10.1039/d6ma00292g

rsc.li/materials-advances

Energy demand in today's world is increasing. So, to meet this energy demand and reduce reliance on fossil fuels, we need to look to renewable energy sources, and hydrogen storage can be one of them. This study conducted a magnificent investigation into the thermo-dynamical stability, optoelectronic properties, hydrogen storage capability, and photocatalytic activity of Li_2XBH_6 (X = Li, Na, K) Double perovskite hydrides (DPH) using a density functional theory (DFT)-based approach, with *ab initio* molecular dynamics (AIMD) simulations, which specifies that the compounds are thermally stable. The electronic structure analysis indicated that all compounds exhibit semiconductor behavior, with band gap energies of 1.79 eV for Li_2LiBH_6, 1.66 eV for Li_2NaBH_6, and 1.48 eV for Li_2KBH_6, suggesting their potential for efficient photonic and optoelectronic applications such as solar cell absorbers. This study shows a prominent initial theoretical GHSC, with Li_2LiBH_6 demonstrating the highest storage potential at 16.05 wt%, Li_2KBH_6 the lowest at 8.66 wt%, and Li_2NaBH_6 11.25 wt% – all considerably surpassing the US-DOE target of ≥5.5 wt%. The study shows that these substances are promising theoretical candidates for advanced optoelectronic devices, hydrogen storage materials, and photocatalytic applications.

1. Introduction

Rising environmental concerns and the ongoing global energy demand have heightened the demand for energy-efficient alternatives to conventional fossil fuels.[1,2] Hydrogen has emerged as a key energy carrier due to its high energy density and potential for direct conversion into mechanical, electrical, and thermal energy.[3,4] However, practical utilization of hydrogen requires the development of a safe, lightweight, efficient, and reversible storage system.[5] There are many hydrogen storage methods, but solid-state storage in complex hydrides has obtained notable recognition due to their high gravimetric hydrogen storage capacity (GHSC), thermodynamic stability, and mechanical reliability.[6,7] Perovskite-type hydrides (ABH_3) represent an encouraging class of materials for solid-state hydrogen storage.[8] Their extensive surface areas enable substantial hydrogen adsorption, while their excellent thermal and chemical stability allows operation under elevated temperatures and harsh chemical environments.[9] There is another advanced subclass of double perovskites, $A_2BB'H_6$, which increases lattice flexibility and enhances mechanical, electronic, and thermodynamic characteristics. Such structural advantages make DPHs particularly suitable for reversible hydrogen storage at moderate temperatures.[10] Releasing hydrogen from a substance is termed desorption.[11] The thermal stability of perovskites makes them well-suited for hydrogen desorption at elevated temperatures. Their outstanding chemical stability makes them suitable for use in corrosive or demanding chemical environments.[12] The ease of manufacture and economic feasibility of these materials increase their suitability for large-scale hydrogen storage applications.[13,14] Though perovskites are seen as a promising solution for hydrogen storage, multiple difficulties must be solved before real-world application.[15] Key obsessions include increasing the kinetics of hydrogen adsorption and desorption, improving the stability and long-term durability of substances under operational conditions, and boosting storage capacity. Because of their magnificent gravimetric hydrogen densities, usually between 1.2 and 6.0 wt%, light metal perovskite hydrides demonstrate strong potential for use in hydrogen storage technologies.[16]

A significant amount of research is currently dedicated to investigating materials for hydrogen storage applications. Researchers are conducting many studies and investigations

[a] *Smart Computing Research Laboratory (SCRL), Department of Electrical and Electronic Engineering, Jatiya Kabi Kazi Nazrul Islam University, Trishal, Mymensingh-2224, Bangladesh. E-mail: shuaib.eee.iu@gmail.com*
[b] *Department of Electrical and Electronic Engineering, Jatiya Kabi Kazi Nazrul Islam University, Trishal, Mymensingh-2224, Bangladesh*
[c] *School of Chemistry and Physics, Queensland University of Technology (QUT), Gardens Point Campus, 2 George Street, Brisbane, QLD 4001, Australia*
[d] *Department of Arts and Sciences, Bangladesh Army University of Science and Technology, Saidpur 5310, Nilphamari, Bangladesh*

on materials to improve H_2 storage capacity. Recent density functional theory (DFT)-based investigations have found that Mn-based hydride single perovskites $KMnH_3$ and $LiMnH_3$ exhibit GHSC of 3.12 and 4.67 wt%, respectively.[17] Similarly, other studies reported GHSC of 7.946, 4.306, 5.588, and 5.456 wt% for $LiSiH_3$, $KSiH_3$, $NaSiH_3$, and $MgSiH_3$.[18] In addition, Cu-based hydrides exhibited relatively lower capacities, namely 3.23 wt% for $AlCuH_3$, 2.22 wt% for $GaCuH_3$, and 1.67 wt% for $InCuH_3$.[19] Extensive investigations into single-perovskite hydrides have provided valuable insights into their hydrogen-storage performance. Specifically, the $NaXH_3$ (X = Be, Mg, Ca, Sr) family exhibits capacities between 2.6 and 8.6 wt%,[20] while $XNiH_3$ (X = Li, Na, K) compounds show values of 3.30–4.40 wt%.[21] Among chalcogen-based hydrides, $LiSH_3$ and $LiSeH_3$ achieve capacities of 7.19 wt% and 3.40 wt%,[22] respectively. Transition-metal-based cesium hydrides demonstrate moderate performance, with $CsCoH_3$ and $CsZnH_3$ offering 2.82 wt% and 3.09 wt%,[23] respectively. But nowadays, DPHs are attracting the attention of researchers because of their greater structural flexibility and improved functionality, as we mentioned before. So, a large number of investigations on DPH are ongoing. In recent times, DFT-based research has found that Cs_2CaCdH_6, Rb_2CaCdH_6, and DPH show GHSC of 1.39 wt% and 1.69 wt%, respectively.[24] DPHs that have already investigated and their GHSCs are 1.78 to 5.39 wt% for X_2CaAlH_6 (X = K, Rb, and Cs),[25] 2.956 wt% for Na_2CaCdH_6,[26] 1.14 and 1.86 wt% for Rb_2AlXH_6 (X = In, Tl),[27] 5.94 and 3.11 wt% for X_2LiBH_6 (X = K, Rb)[28] and 2.40 to 6.39 wt% for A_2LiCuH_6 (A = Be/Mg/Ca/Sr).[29] However, recent DFT investigations on single perovskite hydride and DPHs report GHSCs typically under 8.6 wt%, with most DPHs remaining under 7.05 wt%. These limitations encourage the research of lightweight boron-based DPHs, which remain largely uninvestigated and may enable substantially enhanced hydrogen storage performance.

Most reported studies focus on the individual physical characteristics or hydrogen storage properties of related DPHs. In contrast, a unified evaluation that combines hydrogen storage, optoelectronic, and photocatalytic performance for the Li_2XBH_6 system has not been explored. In this research, we present a comprehensive first-principles investigation of Li_2XBH_6 (X = Li, Na, K) DPHs, highlighting their structural stability, electronic properties, hydrogen storage behavior, and photocatalytic potential using DFT. This provides new information on their structural, optoelectronic, and hydrogen storage characteristics.

In this study, we theoretically present a comprehensive first-principles investigation of Li_2XBH_6 DPHs using DFT coupled with AIMD simulations. We examine their structural stability, electronic properties, hydrogen storage performances, and photocatalytic potential. While experimental synthesis is influenced by precursor choice, chemical purity, and stoichiometric control,[30–32] this theoretical work provides an initial framework for guiding future experimental studies under controlled conditions. Remarkably, these compounds exhibit theoretical GHSCs that exceed the U.S. DOE target and favorable band gap alignments for photocatalytic applications. This work, therefore, provides novel insights into the multifunctional energy potential of Li_2XBH_6 DPHs and establishes a theoretical roadmap for future experimental efforts.

2. Methodology

The first-principles calculations are executed within the DFT framework using the full-potential linearized augmented plane wave (FP-LAPW) method as applied in the WIEN2k computational package,[33,34] which is well-established for accurate treatment of electron interactions in solid-state systems. The exchange–correlation effects for structural and mechanical optimization are treated using the GGA-PBE_{sol} functional,[35] selected for its improved reliability in predicting equilibrium lattice parameters and elastic behavior of perovskite-type hydrides. Recognizing the common tendency of semi-local GGA functionals to underestimate band gaps, the Tran–Blaha modified Becke–Johnson (TB-mBJ) potential is applied to achieve a high-accuracy evaluation of electronic and optical properties with reduced computational cost.[36–38] Brillouin-zone integrations were performed using a Monkhorst–Pack k-point mesh of $12 \times 12 \times 12$ to ensure reliable total-energy convergence. The basis size ($R_{MT} \times K_{max} = 8$), Fourier expansion cutoff charge density ($G_{max} = 13$), charge convergence = 10^{-5} Ry, and energy convergence = 0.0001 eV were set for optimization. To assess the thermal stability of the Li_2XBH_6 (X = Li, Na, K) DPH, AIMD simulations were carried out under constant-temperature conditions, allowing evaluation of structural robustness at elevated temperatures. Highly dense k-point meshes of 5000 and 10 000 points were used to accurately calculate the electronic and optical properties.

The optical parameters were computed from the real $\varepsilon_1(\omega)$ and imaginary part $\varepsilon_2(\omega)$ of dielectric tensor $\varepsilon(\omega)$ and follows:[39–41]

$$n(\omega) = \left(\frac{\varepsilon_1(\omega)}{2} + \frac{\sqrt{\varepsilon_1^2(\omega) + \varepsilon_1^2(\omega)}}{2}\right)^{\frac{1}{2}} \quad (1)$$

$$k(\omega) = \left(-\frac{\varepsilon_1(\omega)}{2} + \frac{\sqrt{\varepsilon_1^2(\omega) + \varepsilon_1^2(\omega)}}{2}\right)^{\frac{1}{2}} \quad (2)$$

$$\alpha(\omega) = \left(\sqrt{2}\right)\left[\sqrt{\varepsilon_1(\omega)^2 + \varepsilon_2(\omega)^2} - \varepsilon_1(\omega)\right]^{\frac{1}{2}} \quad (3)$$

$$\sigma(\omega) = \frac{n(\omega)\alpha(\omega)\omega}{2\pi} \quad (4)$$

$$R(\omega) = \frac{K^2 + (1-n)^2}{K^2 + (1+n)^2} \quad (5)$$

$$L(\omega) = \frac{\varepsilon_2(\omega)}{\varepsilon_1^2(\omega) + \varepsilon_2^2(\omega)} \quad (6)$$

3. Results and discussion

3.1 Structural, mechanical stability, and AIMD simulations

The Double perovskite's general structure is $A_2BB'X_6$,[42] where A, B, and B′ are cations and X is an anion. The structural characteristics of DPH Li_2LiBH_6, Li_2NaBH_6, and Li_2KBH_6 were

examined in detail using first-principles DFT-based computational techniques. This compounds forms crystals with a double perovskite structure that belong to the $Fm\bar{3}m$ space group (no. 225). These structures contain 40 atoms per cubic cell, where Li atoms occupy the Wyckoff position at 8c $\left(\frac{1}{4},\frac{1}{4},\frac{1}{4}\right)$, X atoms are at 4b $\left(\frac{1}{2},\frac{1}{2},\frac{1}{2}\right)$, B atoms occupy 4a (0, 0, 0), and H atoms are at the positions 24e $\left(\frac{1}{4},0,0\right)$. The compounds' lattice properties were optimized by GGA-PBE$_{sol}$, demonstrating a remarkably stable crystal structure in all three materials (Fig. 1). The lattice constants for Li_2LiBH_6, Li_2NaBH_6, and Li_2KBH_6 were 6.2136 Å, 6.8034 Å, and 7.4815 Å, respectively, demonstrating minimal change with increasing cation size, except for potassium, where we observe a noticeable change. From Fig. 2, we found that Li_2LiBH_6 minimizes its overall energy (E_0) at −101.0542 Ry, with a volume (V_0) of 404.7378 bohr^3. For Li_2NaBH_6, at a volume of 531.2702 bohr^3, it minimizes its overall energy at 409.9652 Ry, whereas at a volume of 706.489 bohr^3, Li_2KBH_6 minimizes its overall energy at −1288.2530 Ry. These values are consistent with the expected behavior of perovskite structures, in which greater cations result in greater unit cell diameters. A crystalline material's formation energy, (ΔE_f) offers important information about its primary stability and chemical makeup.[43]

Each one's formation energy was determined using eqn (7):[44]

$$\Delta E_f = E_{total}(Li_2XBH_6) - (2E_{tot}(Li) + E_{tot}(X) + E_{tot}(B) + 6E_{tot}(H)) \quad (7)$$

An element's atomic or molecular arrangement and bonding inside the crystal structure are specified by its formation energy.[43,45] The physical or structural stability factors are:

$$t = \frac{R_A + R_H}{\sqrt{2}\left(\frac{R_B + R_{B'}}{2} + R_H\right)} \quad (8)$$

$$\mu = \frac{R_B + R_{B'}}{2R_H} \quad (9)$$

Here, t refers to the tolerance factor and μ refers to the octahedral factor, and R_A, R_B, $R_{B'}$, and R_H are the corresponding ionic radius of the structures' materials. The tolerance factors,

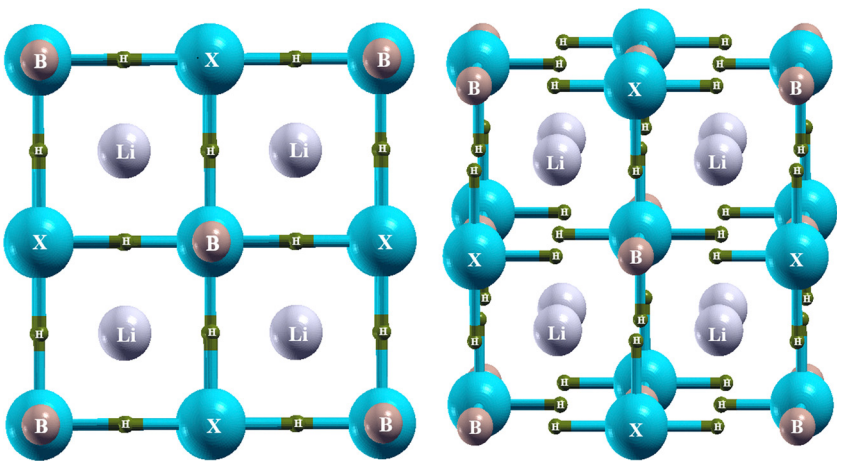

Fig. 1 Unit cell of Li_2XBH_6 (X = Li, Na, K): 2D view shown is on the left side, and 3D view is on the right side.

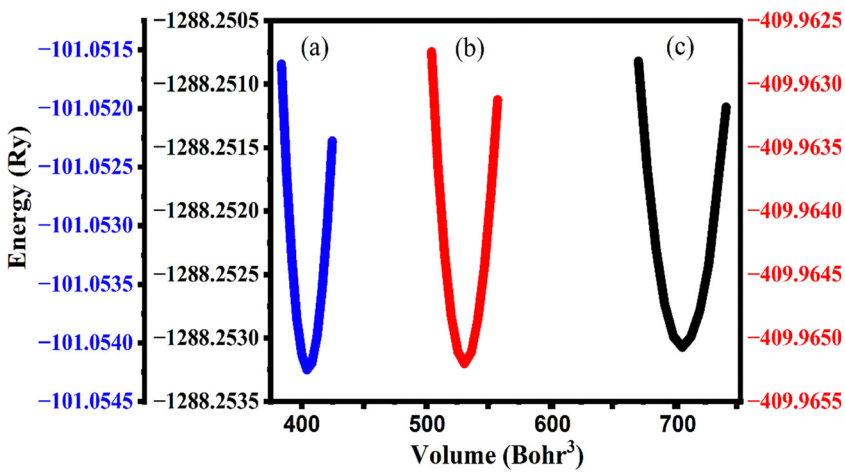

Fig. 2 Energy *vs.* volume graphs of (a) Li_2LiBH_6, (b) Li_2NaBH_6, and (c) Li_2KBH_6 after optimization.

Table 1 The structural properties evaluated for the studied materials

Hydrides	a_0 (Å)	V_0 (bohr^3)	E_0 (Ry)	t	μ	ΔE_f (eV per atom)
Li_2LiBH_6	6.22	404.74	−101.05	0.953	0.37	−2.12
Li_2NaBH_6	6.80	531.27	−409.97	0.892	0.46	−1.96
Li_2KBH_6	7.48	706.48	−1288.25	0.825	0.58	−1.83

which lie within the favorable range of 0.81–1.1,[46] were calculated to be 0.953 for Li_2LiBH_6, 0.892 for Li_2NaBH_6, and 0.825 for Li_2KBH_6. These values imply that the structures are stable and won't distort under typical circumstances.

The bonding environment of the BX_6 octahedra remains favorable for all three compounds, as indicated by the octahedral factors, which were calculated to be 0.37, 0.46, and 0.58, respectively. These values fall within the acceptable range of 0.377 to 0.895[47] (Table 1).

Several numerical experiments on the elastic constants (C_{11}, C_{12}, C_{44}), bulk (B), shear (G), and Young moduli (E), Poisson's ratio (ν), and Pugh's ratio (B/G) are used to confirm their mechanical stability. Stable elastic constants, high stiffness, and resistance to deformation under applied stress are among the materials' advantageous mechanical characteristics. A key consideration for the use of materials in hydrogen storage systems is their mechanical stability, especially for those that are subjected to multiple hydrogen absorption and desorption cycles, as well as for transportation implementation.[48,49] A well-known checklist (Born stability) for determining a material's mechanical soundness uses its elastic constants.[50–53]

$$(C_{11} - C_{12}) > 0, (C_{11} + 2C_{12}) > 0, C_{11} > 0, C_{44} > 0, C_{12} < B < C_{11} \quad (10)$$

Here, B denotes the bulk modulus, and the values of C_{11}, C_{12}, and C_{44} are given in Table 2.

The encouraging outcome of this work is that Li_2LiBH_6 hydride stands out as the one that fully satisfies all the specified criteria. This material is mechanically stable and strong enough to withstand deformation, as demonstrated by its easy compliance with all the requirements. This indicates that it has a robust structure capable of withstanding mechanical stress. In contrast, Li_2NaBH_6 and Li_2KBH_6 do not satisfy the required stability conditions. Therefore, both materials are mechanically unstable, as Li_2NaBH_6 fails to satisfy the conditions $(C_{11} - C_{12}) > 0$, and $C_{12} < B < C_{11}$, while Li_2KBH_6 has a negative C_{11} violating $C_{11} > 0$.

The bulk modulus measures how much a material retains stability under pressure and is used to evaluate both its incompressibility and elasticity.[54] From Table 2, we found that the bulk moduli of Li_2LiBH_6, Li_2NaBH_6, and Li_2KBH_6 are 66.117, 50.067, and 34.757 GPa, respectively, with Li_2LiBH_6 showing the highest bulk modulus. Conversely, the stiffness of a material is characterized by Young's modulus, with higher values indicating increased rigidity.[55] In this study, we found Young's modulus 69.598 GPa for Li_2LiBH_6, 128.382 GPa for Li_2NaBH_6, and 9.119 GPa for Li_2KBH_6. Shear modulus measures a material's resistance to shear, *i.e.*, to shape changes while keeping its volume constant. In relation to other properties, the shear modulus offers a more accurate representation of a material's stiffness.[56] The shear modulus was found to be 26.272 GPa for Li_2LiBH_6, 59.844 GPa for Li_2NaBH_6, and 3.131 GPa for Li_2KBH_6. Poisson's ratio, which indicates a material's degree of ductility, is another important consideration when evaluating its mechanical qualities. The Poisson's ratio for the hydrides under analysis is less than 0.3, which often shows brittle behavior. This indicates that under stress, the materials are more likely to crack than to flex or stretch. This is further confirmed by Pugh's ratio, which shows that the materials are brittle with values below 1.75.[57] From Table 2, we can see that Poisson's ratio (ν) of Li_2LiBH_6, Li_2NaBH_6, and Li_2KBH_6 are 0.325, 0.073, and 0.456, as well as Pugh's ratio (B/G) are 2.517, 0.837, and 11.101, respectively. By analyzing this information, we found that Li_2LiBH_6 and Li_2KBH_6 exhibit ductile behavior, whereas Li_2NaBH_6 is brittle. The Debye temperature (DT) shows how much heat metals can tolerate before melting. By calculating the DT, we found that the DTs of Li_2LiBH_6, Li_2NaBH_6, and Li_2KBH_6 are 921.139 K, 1186.029 K, and 260.910 K, respectively.

The AIMD simulation was performed to evaluate the thermal stability of these compounds.[58] The AIMD simulations were performed at 300, 500, and 800 K, with the smallest variance in fluctuations for the perovskite-type hydrides Li_2KBH_6, Li_2LiBH_6, and Li_2NaBH_6 under the NVE ensemble over a total simulation period of 30 000 fs (Fig. 3). The structural stability of the materials was assessed by analyzing the time-dependent behavior of the total energy and temperature. The energy trends for the three systems show a gradual increase with minor oscillations, indicating that the materials undergo dynamic relaxation in the simulation. Among the studied compounds, Li_2LiBH_6, Li_2NaBH_6, and Li_2KBH_6 show minor energy fluctuations, indicating that their structures are more stable under thermal stress. Throughout the simulation, the temperature profiles for all systems remain stable, fluctuating around 300, 500, and 800 K without notable deviations. The observed consistency demonstrates that the systems effectively maintain thermal equilibrium throughout the NVE ensemble simulation. In summary, the AIMD simulations show that Li_2LiBH_6, Li_2NaBH_6, and Li_2KBH_6 maintain their structural integrity at 300, 500, and 800 K. This stability is comparable to other perovskite hydrides such as $LiZnH_3$, $NaZnH_3$, and $KZnH_3$,[59] where ionic size and lattice flexibility play important roles in determining thermal stability.[60] Therefore, the AIMD results

Table 2 Mechanical properties evaluated for Li_2XBH_6 (X = Li, Na, K) hydrides

Hydrides	C_{11}	C_{12}	C_{44}	B	G	E	ν	B/G	DT
Li_2LiBH_6	75.546	61.403	57.954	66.117	26.272	69.598	0.325	2.517	921.139
Li_2NaBH_6	31.186	59.507	16.261	50.067	59.844	128.382	0.073	0.837	1186.029
Li_2KBH_6	−17.302	60.787	8.572	34.757	3.131	9.119	0.456	11.101	260.910

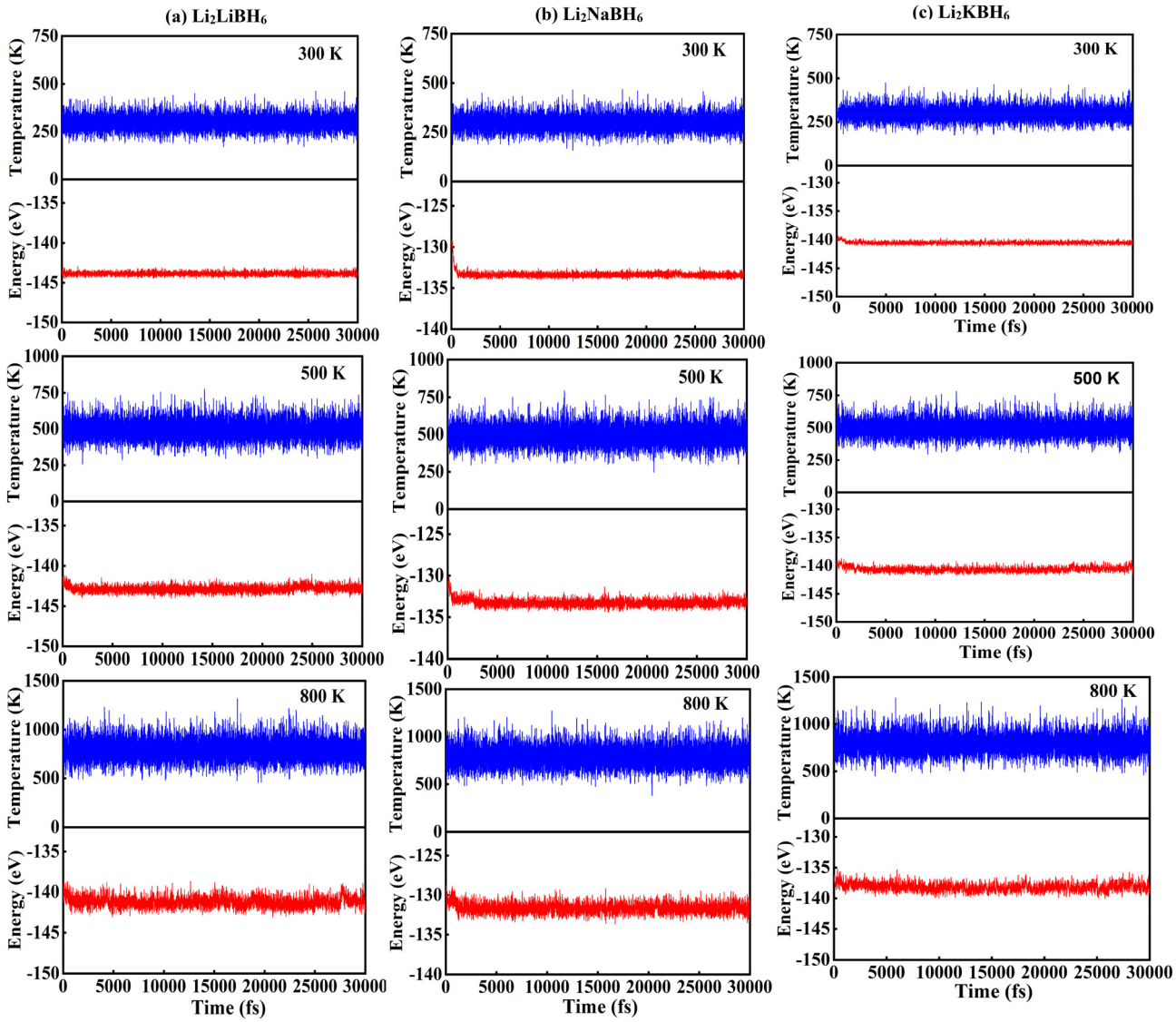

Fig. 3 The AIMD simulation of energy and temperature as a function of time for (a) Li_2LiBH_6, (b) Li_2NaBH_6, and (c) Li_2KBH_6 materials.

confirm the thermal stability of Li_2LiBH_6, Li_2NaBH_6, and Li_2KBH_6 at 300, 500, and 800 K. However, additional structural analyses, such as structural snapshots, radial distribution functions, and mean-square displacement, would be desirable to provide a more comprehensive assessment of long-term thermal behavior.

3.2 Electronic properties

The electronic properties of Li_2XBH_6 (X = Li, Na, K) are analyzed in this work through a comprehensive analysis of the band structure, TDOS, and PDOS. Band structure analysis plays a crucial role in determining a material's electronic properties. We used two methods, GGA-PBE_{sol} and TB-mBJ, to study the band structures and check the accuracy of our results. The band structure of Li_2XBH_6 (X = Li, Na, K) DPH along the *k*-path (W–L–Γ–X–W–K) in the energy range −6 to 6 eV, is shown in Fig. 4, where the left side of the figure shows the approach of the GGA-PBE_{sol} method and the right side shows the TB-mBJ method. The TB-mBJ approximation was employed in this study because of its superior accuracy in estimating band gaps compared to the GGA-PBE_{sol} approach. The TB-mBJ approach produced band gap values that showed close agreement with those reported experimentally.[61] By the GGA-PBE_{sol} method, all three materials exhibit a metallic nature because the valence band and the conduction band overlap. But in the TB-mBJ approach, the compounds exhibit band gap energies of 1.79 eV for Li_2LiBH_6, 1.66 eV for Li_2NaBH_6, and 1.48 eV for Li_2KBH_6. From this observation, we notice that the band gap energy is decreasing with the increase in the size of the X-site atom. In addition, we also observe that the conduction band maximum of all these three compounds is placed at the Γ point, where the red dotted line represents the Fermi energy, and the valence band maximum of these compounds is placed at the X point, except for Li_2KBH_6. Because we found that the valence band maximum of Li_2KBH_6 components is actually placed at the L point, these observations indicate that all of the materials are indirect band gap semiconductors (CBM and VBM at different symmetry

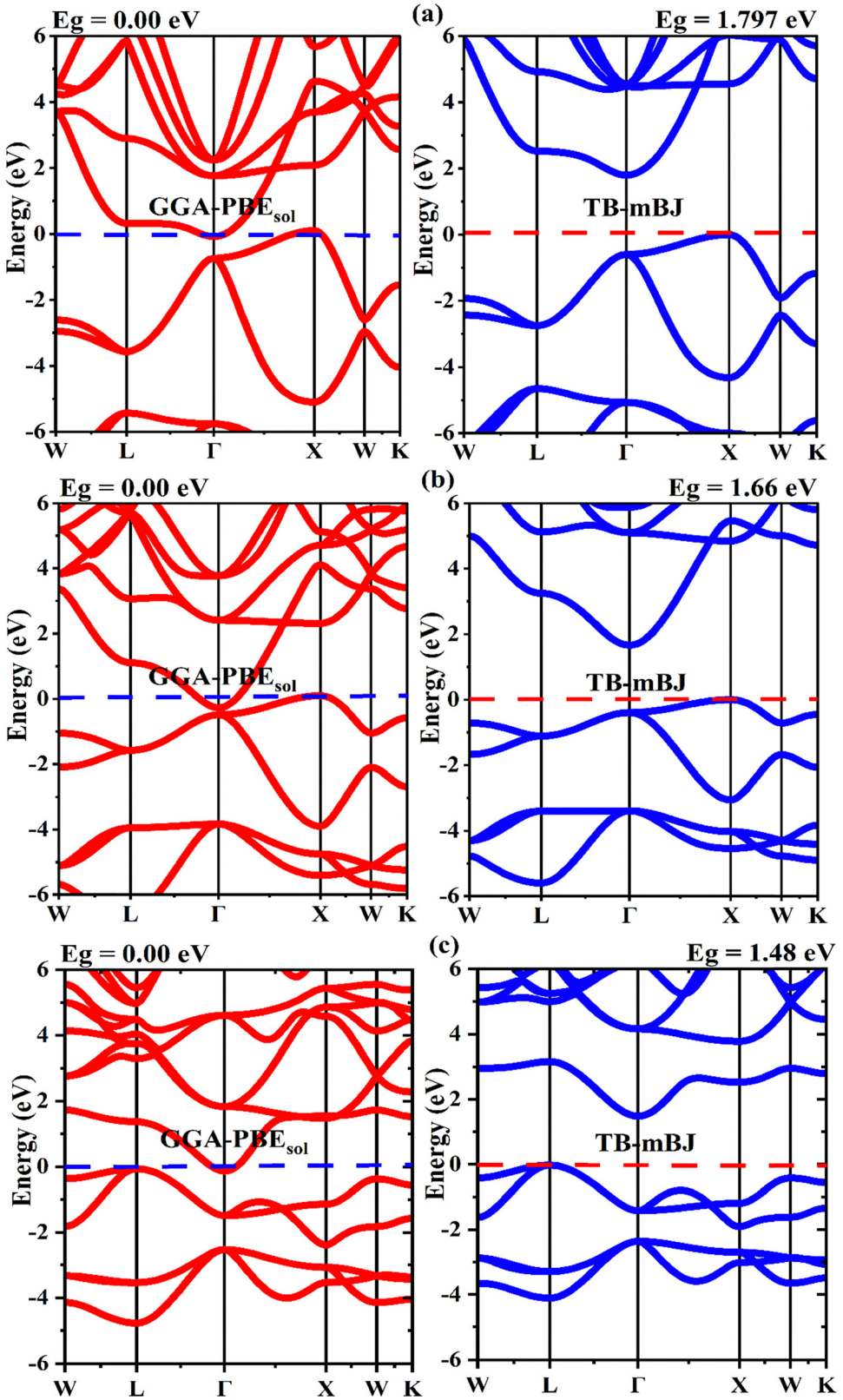

Fig. 4 The electronic band diagram of (a) Li_2LiBH_6, (b) Li_2NaBH_6, and (c) Li_2KBH_6, shown using GGA-PBE$_{sol}$ (on the left side) and TB-mBJ (on the right side) techniques.

points).[62] Therefore, the favorable band gap positions of Li_2XBH_6 (X = Li, Na, K) DPH make them attractive materials for optoelectronic applications such as solar cell absorbers and UV-responsive devices.[63,64]

By studying the DOS and PDOS, we can better understand how electronic states are distributed near the Fermi level, which directly influences conduction and overall electronic properties.[65] So, the density of states (DOS) and partial density

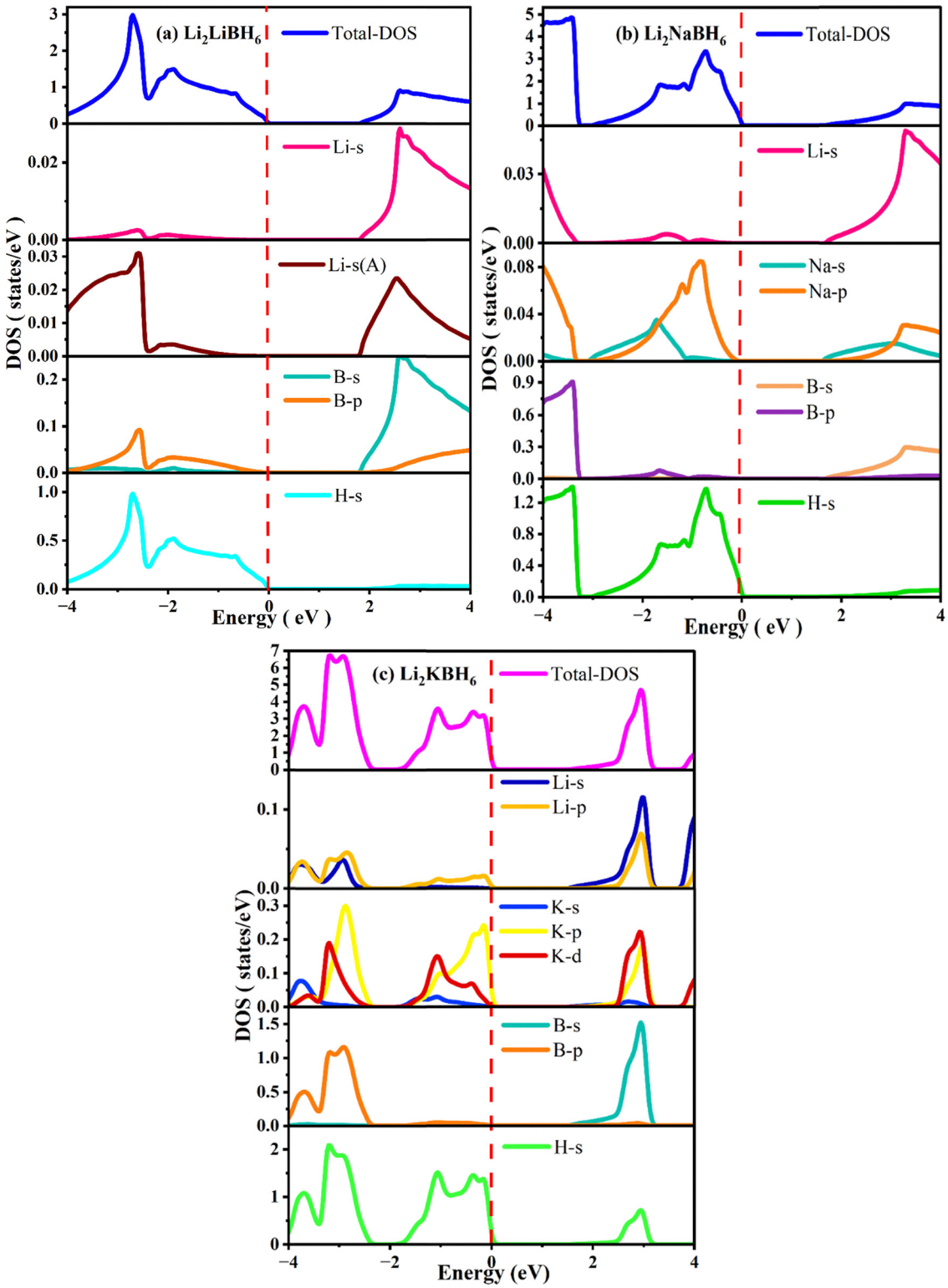

Fig. 5 Total DOS and partial DOS of (a) Li_2LiBH_6, (b) Li_2NaBH_6, and (c) Li_2KBH_6.

of states (PDOS) were also studied for Li_2XBH_6 (X = Li, Na, K) DPH to understand the distribution of electronic states near the Fermi level. Fig. 5 shows the TDOS and PDOS of titled materials, explaining the distribution of electronic states across the conduction and valence bands of the considered compounds. It is found that the total DOS below the Fermi level is higher than that in the conduction band, confirming that hole conductivity is major. In the case of the valence band, hydrogen atoms were found to contribute remarkably to the partial DOS of the Li_2XBH_6 compounds. Therefore, the findings reveal that the electronic states of H^- ions are the major contributors to bonding interactions in these compounds. The strong peaks in H-s within the valence band also refer to the dominance of H_2 states and H^- ions, which act as a significant contributor toward the overall permanence of these compounds. Conversely, the Li atom dominates the conduction band. The contribution of Li-s states in the conduction band is major in all three materials, but B-s states also have a significant role in PDOS. Here, we also found some minor contribution of Na-p in the Li_2NaBH_6 compound, but the contribution of H_2 is minimal in the conduction band, which was the major contributing state in the valence band. Furthermore, we observe that an increase in atomic radius leads to a reduction in the band gap, as the interaction between the nucleus and valence-shell electrons weakens.

In conclusion, the findings indicate that Li-s, B-s, and H-s states dominate the electronic transitions, enabling efficient light absorption and making them suitable for hydrogen storage and optoelectronic devices.

The effective mass of charge carriers significantly influences their mobility and response to external fields, thereby playing a critical role in photovoltaic performance.

The electron (m_e^*) and hole (m_h^*) effective masses were determined from the TB-mBJ band dispersion at the conduction band minimum (Γ point) and valence band maximum (X point and L point for Li_2BH_6) using the parabolic relation:[66]

$$m^* = \frac{\hbar^2}{(d^2E/dK^2)} \quad (11)$$

where $\hbar$ is the reduced Planck constant (1.05×10^{-34} J s^{-1}) and d^2E/dK^2 is the second derivative of the band energy E with respect to the wave vector k.

The exciton binding energy E_b^{ex} is a fundamental parameter governing the efficiency of a material for photovoltaic energy-conversion applications. For high-performance solar cell absorber candidates, this energy must be sufficiently low. A low E_b^{ex} enables excitons (bound electron–hole pairs generated by photo-excitation) to dissociate into free charge carriers (electrons and holes) more efficiently using only the available thermal energy at room temperature. This directly improves charge transport, enhances carrier mobility, and suppresses recombination loss. Conversely, excessively high exciton binding energy hinders dissociation, leading to reduced charge-carrier mobility and elevated recombination rates, which critically degrade solar-cell efficiency and device performance. Excitonic effects originate from the coulombic attraction between photo-excited electron–hole pairs inside the crystal lattice.

In this work, the exciton binding energies of the Li_2XBH_6 family (X = Li, Na, K) were estimated using the Wannier–Mott exciton model, involving the carrier reduced mass and static dielectric response of the respective compounds. The model applied for E_b^{ex} evaluation follows the hydrogenic formalism:[66]

$$E_b^{ex} = \frac{\mu_r e^4}{32(\pi\epsilon_0\hbar^2\epsilon_r)^2} = 13.56\frac{\mu_r}{m_e\epsilon_1(0)^2} \quad (12)$$

where the reduced effective mass (μ_r) was calculated as

$$\mu_r = \frac{m_e^* m_h^*}{m_e^* + m_h^*} \quad (13)$$

The density-of-states effective masses and the corresponding effective density of states in the valence band (N_v) and conduction band (N_c).

These are key parameters that determine the intrinsic carrier concentration and thereby influence the electrical transport and optoelectronic performance of semiconductors. Using the calculated electron (m_e^*) and hole (m_h^*) effective masses, the density-of-states effective masses were evaluated, and the effective densities of states at 300 K were computed using the well-established expressions:[67]

$$N_v = 2\frac{(2\pi m_h^* k_B T)^{3/2}}{h^3} \approx 2.5409 \times 10^{19}\left(\frac{m_h^*}{m_0}\right)^{3/2} \quad (14)$$

$$N_c = 2\frac{(2\pi m_e^* k_B T)^{3/2}}{h^3} \approx 2.5409 \times 10^{19}\left(\frac{m_e^*}{m_0}\right)^{3/2} \quad (15)$$

where k is Boltzmann's constant, h is Planck's constant, and T is the absolute temperature.

The electron and hole carrier mobilities (μ_h and μ_e) were estimated using the effective mass approximation by assuming a relaxation time of $\tau = 10^{-14}$ s. The mobilities were calculated using the following expressions:[68]

$$\mu_h = \frac{q\tau}{m_h^*}, \quad \mu_e = \frac{q\tau}{m_e^*}$$

where q denotes the elementary charge 1.6×10^{-19} C. The calculated carrier mobility from Table 3 show that electron transport is more favorable than hole transport in all three components, as μ_e is consistently higher than μ_h. Among them, Li_2KBH_6 shows the highest electron mobility, whereas Li_2LiBH_6 shows the highest hole mobility, suggesting promising charge-transport characteristics for optoelectronic applications, as well as Li_2LiBH_6 exhibits a flat band-edge profile, indicating a lower degree of band dispersion near the valence and conduction band extrema. In contrast, Li_2NaBH_6 and Li_2KBH_6 show comparatively strong curved bands, reflecting higher dispersion.

3.3 Optical properties

A comprehensive understanding of a material's optical properties is essential for its interaction with electromagnetic radiation and for its usefulness in optoelectronic and photovoltaic

Table 3 Electronic parameters of Li_2XBH_6 (X = Li, Na, K) compounds, including TB-mBJ band gaps, effective masses, density-of-states effective densities (N_c, N_v), and exciton binding energies

Compound	TB-mBJ (eV)	Nature	m_h^*/m_0	m_e^*/m_0	N_v	N_c	μ_h (cm^2 V^{-1} s^{-1})	μ_e (cm^2 V^{-1} s^{-1})	E_b^{ex}
Li_2LiBH_6	1.79	Indirect	0.23	0.19	2.77×10^{18}	2.08×10^{18}	76.37	92.45	0.08
Li_2NaBH_6	1.66	Indirect	0.33	0.13	4.76×10^{18}	1.18×10^{18}	53.23	135.12	0.11
Li_2KBH_6	1.48	Indirect	0.27	0.11	3.52×10^{18}	9.16×10^{17}	65.06	159.68	0.06

devices. Some of the important optical parameters that are crucial for understanding the role of Li_2XBH_6 (X = Li, Na, K) with respect to incident photon flux and their use in various electronic devices, coatings, solar cells, as well as hydrogen storage applications include the dielectric functions, refractive indices, absorption coefficients, extinction coefficients, reflectivity, and optical conductivities.[69] These are determined by the complex dielectric function given by:[70,71]

$$\varepsilon(\omega) = \varepsilon_1(\omega) + i\varepsilon_2(\omega) \quad (16)$$

The real part, $\varepsilon_1(\omega)$, indicates the material's ability to get polarized in the presence of the external electromagnetic field, thereby allowing it to get information about the refractive properties of the material. On the other hand, the imaginary part $\varepsilon_2(\omega)$, is indicative of the material's extinction properties.[72] From Fig. 6(a) and (b), the static dielectric constants for Li_2XBH_6 are ~4.00, which are recorded well with cations (Li, K) providing strong polarization response, and 3.3 for Li_2NaBH_6, ensuring intermediate polarization collapse. In the visible region, all compounds feature relatively small but distinct peak features at around 2.6 eV for Li_2KBH_6, and some further fall-off $\varepsilon_1(\omega)$ reaching maxima between about 5 and 7.5 eV in the ultraviolet (UV). For $\varepsilon_2(\omega)$, negligible contributions are found at zero photon energy, whereas a small peak is again visible for Li_2KBH_6 at 3.2 eV in the visible range, with the maximum absorption occurring in the UV region for all

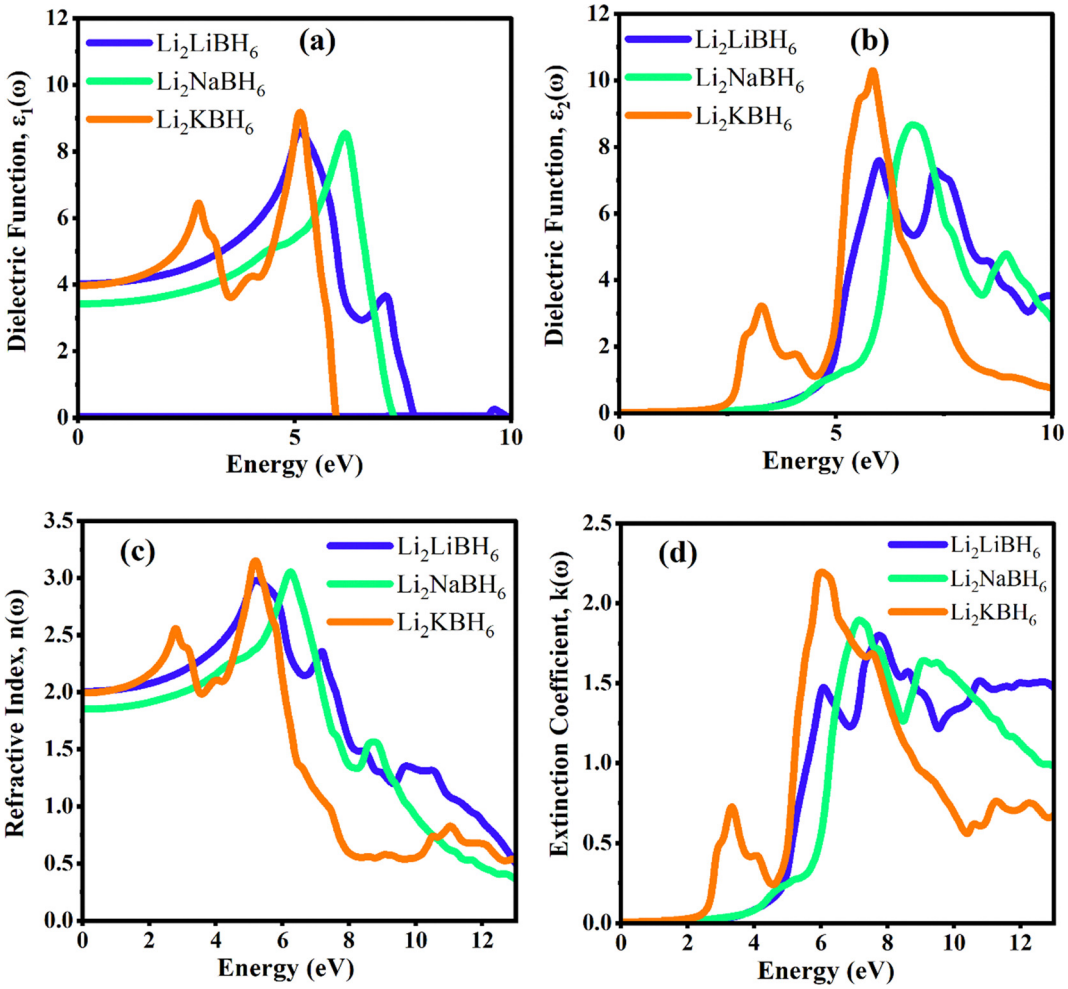

Fig. 6 (a) Real dielectric function, $\varepsilon_1(\omega)$, (b) imaginary dielectric function, $\varepsilon_2(\omega)$, (c) refractive index, $n(\omega)$, and (d) extinction coefficient, $k(\omega)$ for Li_2XBH_6 (X = Li, Na, K) materials.

compounds.[73] These results are consistent with the Penn model, which empirically correlates the static dielectric constant with the optical band gap, expressed as:[66]

$$\epsilon_1(0) \approx 1 + \left[\frac{\hbar\omega_p}{E_g}\right]^2 \quad (17)$$

Here, the reasonable values of $\varepsilon_1(0)$ align with the relatively wide band gaps of Li_2XBH_6 compounds and reflect the reduced polarizability expected for materials with high-energy interband transitions. This behavior also suggests that the dielectric response is slightly increased as the effective band gap decreases (as in Li_2KBH_6), which agrees with Penn's model. The real part $n(\omega)$ and the imaginary part $k(\omega)$ in Fig. 6(c) and (d) have similar trends to those of the dielectric function, according to the optical relation $n^2(\omega) = \varepsilon_1(\omega)$.[74,75] At zero photon energy, $n(0)$ lies between 1.8 for Li_2NaBH_6 and 2.0 for Li_2LiBH_6 and Li_2KBH_6 compositions. Both $n(\omega)$ and $k(\omega)$ increase steadily into the UV region, where they reach their maxima. The visible region shows a distinct peak for Li_2KBH_6, indicating a stronger optical response to the Li- and Na-based materials.

Fig. 7(a) depicts that the maximum absorption coefficients for Li_2LiBH_6, Li_2NaBH_6, and Li_2KBH_6 are approximately 1.99×10^6 cm^{-1}, 1.57×10^6 cm^{-1}, and 1.37×10^6 cm^{-1} occurring at photon energies of 12 eV, 9.8 eV, and 6 eV, respectively, which measures how efficiently incoming photons drive electronic transitions from the valence to the conduction band.[76] All the compounds exhibit strong absorption in the UV region, consistent with their characteristic as wide-band-gap semiconductors. Li_2KBH_6 is the only compound that exhibits an additional, but smaller, absorption coefficient of 2.61×10^5 cm^{-1} at 3.2 eV in the visible spectrum, indicating better light-harvesting properties compared to the other compounds. The other Li and Na-based compounds also show an absorption peak (10^3 to 10^4 orders) in the visible range of 1.77 to 3.26 eV. Therefore, the studied materials may be used as the absorbing layer of a solar cell, as a silicon solar cell captures the absorption coefficients of 10^3 to 10^5 orders.[77] The optical conductivity $\sigma(\omega)$ in Fig. 7(b), showing the shape typical of their absorption process, exactly like the real space coupling between the photon absorption and the charge carriers' excitation. In the low-energy region, all three materials exhibit nearly no conductance, which becomes

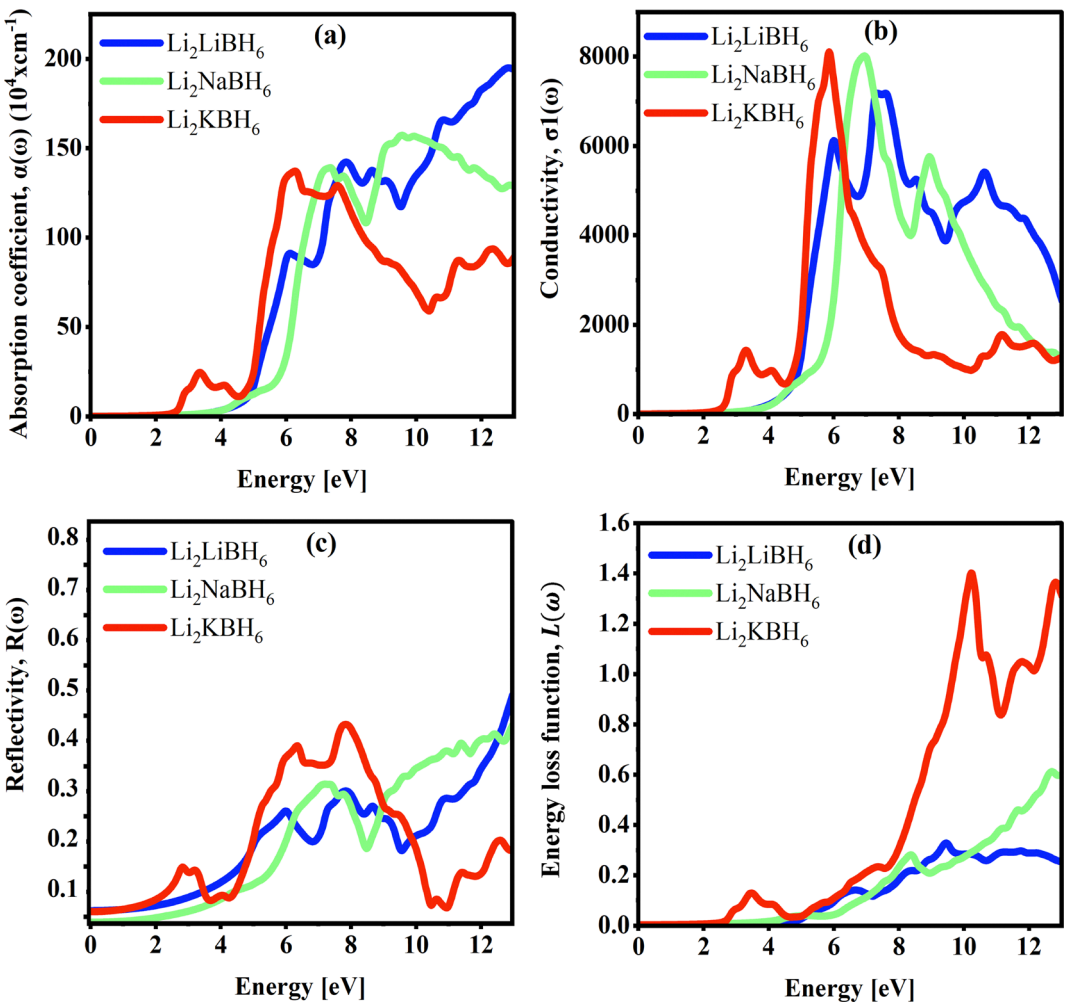

Fig. 7 (a) Absorption, $\alpha(\omega)$, (b) conductivity, $\sigma(\omega)$, (c) reflectivity, $R(\omega)$, (d) energy loss function, $L(\omega)$ for Li_2XBH_6 (X = Li, Na, K) materials.

appreciable around 4–5 eV where interband transitions set in. The main conductivity peaks are concentrated in the ultraviolet (UV) region, which presents a great number of open electronic states. Among the studied systems, Li_2NaBH_6 achieves both the highest peak and the smallest half-width, whereas a similarly strong but broader response is seen for Li_2LiBH_6. In contrast, a significant feature is observed for Li_2KBH_6, which does reach into the visible region, in agreement with its previously observed weak absorption in this range. The general tendency also indicates that the higher absorption of the larger population of photo-generated charge carriers causes an increase. The increased optical conductivity value that diminishes the reflection capabilities and enables efficient energy transfer within optoelectronic devices further emphasizes Li_2XBH_6 compounds as a potential system for light-driven applications.[78]

Fig. 7(c) depicts the reflectivity spectra $R(\omega)$ of the Li_2XBH_6 (X = Li, Na, K) compounds in percent to evaluate their surface photon-reflection response. All are characterized by low reflectivity in both low energy and visible (typically less than 15 percent), meaning not all incident light is reflected from the surface.[79] The low reflectance facilitates enhanced light absorption, which is beneficial for optoelectronics and photovoltaics. As photon energy increases into the UV, reflectivity is more significantly enhanced across all compositions. The highest responses are observed at Li_2KBH_6, with peaks around 35–45%, while for Li_2LiBH_6 and Li_2NaBH_6, they are in the 20–30% range. This behavior indicates that Li_2XBH_6 (X = Li, Na, K) has low reflectivity in the visible but strong reflectivity in the UV, due to high-energy interband transitions. Fig. 7(d) shows the energy loss function, $L(\omega)$ (e-loss), which represents the energy lost by fast electrons traversing the material and is closely related to plasmonic excitations. The collective electronic excitations in the Li_2XBH_6 compounds exhibit well-defined trends in their e-loss spectra. Li_2KBH_6 shows a much-enhanced e-loss peak, approximately an order of magnitude higher, reaching about 1.4, compared to Li_2LiBH_6 and Li_2NaBH_6, with maximum values around 0.4 and $\sim$0.3, respectively. Such a strong peak in Li_2KBH_6 implies enhanced plasmon resonance and a higher probability of inelastic electron scattering, leading to more energy dissipation inside the lattice. The progressively increasing extremum e-loss values at higher energies also demonstrate the increasing density of accessible unoccupied states involved in plasmonic excitations.[80] Therefore, the studied materials may serve as the absorbing layer of a solar cell due to their low reflectivity, appreciable absorption in the visible range, and bandgap values close to the S.Q. limit,[81] although their optical response remains more pronounced in the UV region.

3.4 Hydrogen storage properties

The primary challenge in utilizing hydrogen is the absence of efficient storage materials, but researchers have developed structures capable of storing high hydrogen concentrations reversibly.[82,83] In the near future, the demand for hydrogen storage as a renewable energy source will increase significantly. Volumetric hydrogen storage capacity is an important consideration for hydrogen storage. To determine whether these materials can be used in hydrogen storage technology, the following equations are used:[84]

$$C\ \mathrm{wt}\% = \left[\left\{\frac{\left(\frac{H}{M}\right)m_{\mathrm{H}}}{m_{\mathrm{host}} + \left(\frac{H}{M}\right)m_{\mathrm{H}}}\right\} \times 100\right]\% \quad (18)$$

where, m_{host} is the molar mass of the host material, H/M is the atomic ratio of hydrogen to the host material, and m_{H} is the molar mass of hydrogen. The initial theoretical gravimetric hydrogen storage capacity (GHSC) of Li_2LiBH_6 is 16.05 wt%, where Li_2NaBH_6 is 11.25 wt%, and Li_2KBH_6 is 8.66 wt%. Hydrogen desorption is the mechanism by which hydrogen is liberated from a substance. Since lower desorption temperatures are more practical for real-world applications, they are considered highly desirable. Favorable hydrogen desorption temperatures (T_{des}) typically lie in the range of 450–650 K.[85] For determining the desorption temperature, which equation must be used:

$$2\mathrm{LiH} + \mathrm{XH} + \mathrm{B} + \frac{3}{2}\mathrm{H_2} \rightarrow \mathrm{Li_2XBH_6} \quad (19)$$

The T_{des} can be calculated by the Gibbs reaction[86,87]

$$\Delta G = \Delta H - T_{\mathrm{des}}\Delta S \quad (20)$$

$$\Delta T_{\mathrm{des}} = \frac{\Delta H}{\Delta S} \quad (21)$$

Here, ΔH denotes the formation enthalpy, whereas ΔS indicates the enthalpy change of hydrogen, which is $-130\ \mathrm{J\ mol^{-1}\ K^{-1}}$.[88] The calculated T_{des} of Li_2LiBH_6, Li_2NaBH_6, and Li_2KBH_6 are 521.67, 482.30, and 451.18 K, respectively, which lie within an optimal range, supporting their potential for controlled hydrogen release in an energy system.

Hydrogen storage performance can't be evaluated solely based on theoretical gravimetric capacity, because practical hydrogen release is also governed by thermodynamic stability, decomposition pathway, intermediate phase formation, desorption kinetics, and reversibility. In complex hydrides, hydrogen desorption generally occurs *via* thermally activated bond breaking and often proceeds through multistep reactions rather than a single ideal step. For comparison, MgH_2 is a well-known hydride with a theoretical hydrogen capacity of about 7.6%, but its practical deployment is limited by relatively high desorption temperature and slow reaction kinetics. Likewise, $NaAlH_4$ exhibits a theoretical capacity of about 5.6% and releases hydrogen through multistep decomposition involving intermediate phases such as Na_3AlH_6,[89] while $LiBH_4$, despite its very high theoretical hydrogen capacity, remains challenged by strong thermodynamic stability and sluggish dehydrogenation behavior.[90] Compared with these experimentally established hydrides, the Li_2XBH_6 compound investigated here shows encouraging theoretical gravimetric capacities and favorable desorption characteristics. Nevertheless, their practical hydrogen-storage applicability can't yet be confirmed, and further experimental studies on decomposition pathways, kinetic barriers, and cycling reversibility are required.

A comparison of our materials in Table 4 with other reported DPHs shows that Li_2XBH_6 compounds exhibit significantly higher GHSC. Notably, the Li_2LiBH_6 compound exhibits an exceptionally high hydrogen storage capacity of 16.05%, exceeding both previously reported materials and the U.S.DOE target, while maintaining a practical T_{des} below 650 K. Conclusively, these properties make this material convincing for future hydrogen storage applications.

3.5 Photo-catalytic properties

The photocatalytic activities of Li_2LiBH_6, Li_2NaBH_6, and Li_2KBH_6 are primarily assessed by their ability to absorb sunlight, the appropriateness of their band gaps, the positions of their band edge levels, and their optical absorption features. According to the thermodynamic theory, the alignment of the potential distribution of a photocatalyst and band gap, that is, a band gap of at least 1.23 eV, or more practically, of ~1.5 eV, is both a necessary and sufficient prerequisite to water splitting in the sun.[99,100] On the other hand, H_2O oxidation and reduction are multi-step processes, with the former a four-electron reaction and the latter a two-electron reaction.

$$2H_2O \rightarrow O_2 + 4H^+ + 4e^-$$

$$4H^+ + 4e^- \rightarrow 2H_2$$

During the electron transfer process, an activation barrier separates the water molecules from the photocatalyst. This resistance causes the water oxidation and reduction reactions to require a significant overpotential, meaning that incident photons must have energies above the photocatalyst's band gap to effectively drive the reactions. As a result, the lower band gap should be significantly larger than 1.23 eV to fully split water. To utilize the visible light and maximize solar energy, the band gap must be smaller than 3.0 eV.[101] To analyze the potential of perovskites as photocatalysts, the Mulliken electronegativity approach was employed to investigate their photocatalytic activity. Mulliken defined the electronegativity of an atom as the arithmetic mean of its atomic electron affinity (A_f) and first ionization energy (I_1).[102]

$$\chi_{atom} = \frac{(A_f + I_1)}{2} \quad (22)$$

For a compound with 4 elements, a, b, c, and d, with numbers of atoms p, q, r, and s respectively, for each.[103,104] The electron negativity for a compound can be calculated using eqn (23) as:

$$\chi_{GM} = \left(\chi_a^p \times \chi_b^q \times \chi_c^r \times \chi_d^s\right)^{\frac{1}{p+q+r+s}} \quad (23)$$

Mulliken's electronegativity approach was used in calculating the band edge potentials (E_{CBM} and E_{VBM}), and they are expressed as:[105]

$$E_{CBM} = \chi_{GM} - E_0 - \frac{E_g}{2} \quad (24)$$

$$E_{VBM} = \chi_{GM} - E_0 + \frac{E_g}{2} \quad (25)$$

where χ_{GM} is the absolute electronegativity of the material (the geometrical mean of the Mulliken electro-negativities),[106] E_g is the band gap (TB-mBJ), E_0 energy of free electrons relative to NHE (normal hydrogen electrode) is approximately 4.5 eV, E_{CBM} is the potential of the conduction band minima (CBM), and E_{VBM} is the potential of the valence band maxima (VBM).

To be successful in photocatalytic water splitting, a semiconductor must fulfill two conditions: (1) the valence band maximum of the semiconductor must be more positive than the potential edge of H_2O/O_2, and (2) the conduction band minimum of the semiconductor must be more negative than the redox potential of H^+/H_2 (0 V *vs.* NHE).[107] It is observed that the compounds have band gaps ranging from 1.23 to 3 eV in the visible light spectrum. Indirect band gaps reduce the rate of recombination and carrier lifetimes, which are beneficial in photocatalytic surface reactions.[108] The VBM values of all three compounds are more positive than that of H_2O/O_2 (greater than +1.23 V *vs.* NHE), while their CBM values are more negative than the redox potential of H^+/H_2 (0 V *vs.* NHE). This indicates that the compounds possess strong oxidative and reductive properties, making them highly effective for water oxidation. For the Li_2XBH_6 (X = Li, Na, K) compounds, Li_2LiBH_6 exhibits edge potentials of +1.65 V for the VBM and −0.15 V for the CBM. Similarly, Li_2NaBH_6 shows edge potentials of +1.55 V (VBM) and −0.11 V (CBM), while Li_2KBH_6 presents +1.38 V (VBM) and −0.10 V (CBM). The indirect band gaps of Li_2NaBH_6 and Li_2KBH_6 are relatively narrow, and their conduction band edges lie close to the CO_2 reduction potential for CO formation in the light spectrum. Moreover, the conduction bands of all three compounds are positioned near the CO_2 reduction potential for HCOOH production, indicating a high potential of visible-light-driven CO_2 photo reduction, and in particular when combined with co-catalysts to enhance the efficiency of charge separation.[109,110] For better context, the predicted photocatalytic behavior of Li_2XBH_6 may be compared with well-known photocatalysts such as TiO_2 and g-C_3N_4.[111,112] TiO_2 is a classical photocatalyst with strong redox capability, but its activity is mainly restricted to the UV region because of

Table 4 Band gap, GHSC, (Cwt%), and desorption temperature, (T_{des}) of present and reported work

Hydrides	Band gap (eV)	C wt%	T_{des} (K)	Ref.
Li_2LiBH_6	1.79	16.05	521.67	This work
Li_2NaBH_6	1.66	11.25	482.30	This work
Li_2KBH_6	1.48	8.66	451.18	This work
MgH_2	—	7.6	~673–723	91
$NaAlH_4$	—	5.6	~463–498	92
Na_2LiAlH_6	5.20	7.05	373.9	93
K_2LiAlH_6	2.904	5.08	360.2	94
Na_2LiGaH_6	3.41	4.71	337.1	93
K_2LiGaH_6	1.451	3.71	241.3	94
Na_2CaCdH_6	2.08	2.95	—	95
Rb_2NaAlH_6	3.88	2.30	215.78	96
Rb_2NaInH_6	2.81	2.01	175.63	96
Rb_2CaCdH_6	2.30	1.69	—	97
Ba_2LiNbH_6	0.95	1.59	—	98

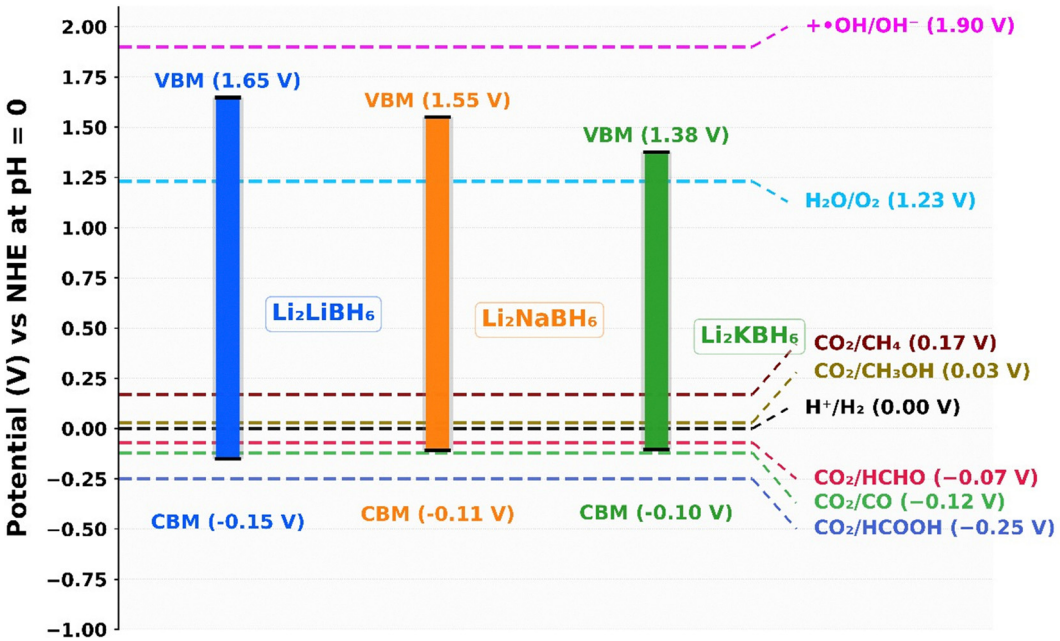

Fig. 8 Calculated edge potentials *vs.* NHE of Li_2XBH_6 (X = Li, Na, K) with respect to the reduction and oxidation potentials of H_2O at pH = 0.

its wide band gap. In contrast, g-C_3N_4 has a narrower band gap and is widely investigated for visible-light photocatalysis. Compared with these benchmark systems, the Li_2XBH_6 compounds (Fig. 8) show theoretically favorable band-edge positions for water splitting, indicating their potential as promising photocatalytic materials. On the other hand, the VBM values lie slightly below the $^{\bullet}OH/OH^{-}$ potential (1.90 V *vs.* NHE), indicating that they are not sufficiently positive to drive oxidation, and their VBMs can drive strong water oxidation under visible light, while their CBMs are promising candidates for water reduction in the visible light spectrum. This study is entirely theoretical, and further experimental investigations will be conducted in the future to validate these results.

4. Conclusion

Li_2LiBH_6, Li_2NaBH_6, and Li_2KBH_6 exhibit remarkable solid-state structural and Thermodynamic stability for multifunctional applications such as significant theoretical hydrogen storage capabilities and photocatalytic applications. However, in the case of mechanical stability, only Li_2LiBH_6 satisfies the required criteria, whereas Li_2NaBH_6 and Li_2KBH_6 fail to meet those conditions. Among these, Li_2LiBH_6 demonstrates the highest initial effectiveness, exhibiting a remarkable theoretical GHSC of 16.05 wt% and a T_{des} of 521.67 K. Li_2NaBH_6 and Li_2KBH_6 also meet the U.S. DOE hydrogen storage benchmarks, exhibit considerable storage capacities of 11.25 and 8.66 wt%, and desorption temperatures of 482.30 and 451.18 K that lie within the operational range. They also display semiconducting nature, creating opportunities for advanced optoelectronic systems. Additionally, these hydrides' optical absorption characteristics also point to possible applications in photovoltaics and other optoelectronic domains. Moreover, CBM of all three compounds is more negative than 0 V *vs.* NHE, while VBM is more positive than +1.23 V *vs.* NHE. This alignment indicates strong oxidation and reduction potentials, respectively, rendering these materials suitable for photocatalytic applications. In conclusion, this study shows that the materials are promising for hydrogen storage and photocatalytic applications.

Author contributions

Partha Podder: writing – original draft, methodology, formal analysis, data calculations, validation. **Joy Kumar Sharkar**: writing – original draft, methodology, formal analysis, data calculations, validation. **Md. Al-Amin**: writing – review & editing, investigation, validation. **R. M. Tanvir**: writing – review & editing, investigation, validation. **Siyam Sheikh**: writing – review & editing, validation. **Md Tarikal Nasir**: writing – review & editing, validation. **A. Rayhan**: writing – review & editing, validation. **S. Mahmud**: conceptualization, formal analysis, methodology, validation, writing – review & editing, software, supervision, project administration.

Conflicts of interest

The authors declare that they have no known competing financial interests or personal relationships that could have appeared to influence the work reported in this paper.

Data availability

The datasets used and/or analysed during the current study are available from the corresponding author on reasonable request.

Acknowledgements

The authors gratefully acknowledge the Smart Computing Research Laboratory (SCRL), Department of Electrical and Electronic Engineering, Jatiya Kabi Kazi Nazrul Islam University (JKKNIU), Mymensingh-2224, Bangladesh, for providing the computational facilities and support essential to the completion of this work.

References

1 A. Züttel, Hydrogen storage methods, *Naturwissenschaften*, 2004, **91**, 157–172.
2 J. Graetz, New approaches to hydrogen storage, *Chem. Soc. Rev.*, 2008, **38**, 73–82.
3 S. E. Hosseini and M. A. Wahid, Hydrogen production from renewable and sustainable energy resources: promising green energy carrier for clean development, *Renewable Sustainable Energy Rev.*, 2016, **57**, 850–866.
4 S. E. Hosseini and M. A. Wahid, Hydrogen from solar energy, a clean energy carrier from a sustainable source of energy, *Int. J. Energy Res.*, 2020, **44**, 4110–4131.
5 L. Zhou, Progress and problems in hydrogen storage methods, *Renewable Sustainable Energy Rev.*, 2005, **9**, 395–408.
6 M. Baaddi, *et al.*, The effect of strain on hydrogen storage characteristics in K_2NaAlH_6 double perovskite hydride through first principle method, *Environ. Sci. Pollut. Res.*, 2024, **31**, 62056–62064.
7 M. Tahir, M. Usman, J. U. Rehman and M. B. Tahir, A first-principles study to investigate the physical properties of Sn-based hydride perovskites $XSnH_3$ (X = K, Li) for hydrogen storage application, *Int. J. Hydrogen Energy*, 2024, **50**, 845–853.
8 S. Zafar, I. Zeba and S. S. A. Gillani, Probing ion substitution in $NaAlO_{3-x}H_x$ perovskites for advanced hydrogen storage systems: a prediction through DFT, *Int. J. Hydrogen Energy*, 2024, **94**, 285–299.
9 M. Ostadebrahim and O. Moradlou, Electrochemical hydrogen storage in $LaMO_3$ (M = Cr, Mn, Fe, Co, Ni) nano-perovskites, *J. Energy Storage*, 2023, **72**, 108284.
10 A. Obeidat, A. Alrousan and S. Abu-Rajouh, First-principles study of structural, hydrogen storage, mechanical, electronic, and optical properties of K_2NaXH_6 (X = Al, As, Bi, Ga, In) double perovskite hydrides, *J. Power Sources*, 2025, **642**, 236944.
11 C. Motta, *et al.*, Revealing the role of organic cations in hybrid halide perovskite $CH_3NH_3PbI_3$, *Nat. Commun.*, 2015, **6**, 1–7.
12 L. Zhu, *et al.*, Graded interface engineering of 3D/2D halide perovskite solar cells through ultrathin $(PEA)_2PbI_4$ nanosheets, *Chin. Chem. Lett.*, 2021, **32**, 2259–2262.
13 W. Feng, *et al.*, Perovskite crystals redissolution strategy for affordable, reproducible, efficient and stable perovskite photovoltaics, *Mater. Today*, 2021, **50**, 199–223.
14 Y. Zhang, S. G. Kim, D. K. Lee and N. G. Park, $CH_3NH_3PbI_3$ and $HC(NH_2)_2PbI_3$ Powders Synthesized from Low-Grade PbI_2: Single Precursor for High-Efficiency Perovskite Solar Cells, *ChemSusChem*, 2018, **11**, 1813–1823.
15 M. Simanullang and L. Prost, Nanomaterials for on-board solid-state hydrogen storage applications, *Int. J. Hydrogen Energy*, 2022, **47**, 29808–29846.
16 R. M. A. Khalil, S. Hayat, M. I. Hussain, A. M. Rana and F. Hussain, DFT-based first principles study of novel combinations of perovskite-type hydrides $XGaH_3$ (X = Rb, Cs, Fr) for hydrogen storage applications, *AIP Adv.*, 2021, **11**, DOI: 10.1063/5.0037790.
17 M. Usman, D. Pan, M. K. Masood and C. Zhang, Mn-based hydride perovskites $XMnH_3$ (X = K, Li): a DFT study for physical properties, and hydrogen storage capability, *Solid State Commun.*, 2024, **390**, 115600.
18 A. Mera and M. A. Rehman, First-principles investigation for the hydrogen storage properties of $AeSiH_3$ (Ae = Li, K, Na, Mg) perovskite-type hydrides, *Int. J. Hydrogen Energy*, 2024, **50**, 1435–1447.
19 R. M. Tanvir, S. Tanvir, M. Al-Amin, A. Rayhan and S. Mahmud, Computational analysis of hydrogen storage and physical behavior of Al, Ga, and In-based Copper hydrides, *Comput. Condens. Matter*, 2025, **45**, e01175.
20 D. Tufail, U. Ahmed, M. Haleem, B. Amin and M. Shafiq, DFT study of alkaline earth metals $NaXH_3$ (X = Be, Mg, Ca, Sr) for hydrogen storage capacity, *RSC Adv.*, 2025, **15**, 337–347.
21 A. Gencer and G. Surucu, Investigation of structural, electronic, and lattice dynamical properties of $XNiH_3$ (X = Li, Na, and K) perovskite-type hydrides and their hydrogen storage applications, *Int. J. Hydrogen Energy*, 2019, **44**, 15173–15182.
22 A. M. Ali, *et al.*, A DFT investigation of Li-based hydride perovskites $LiXH_3$ (X = S, Se) for hydrogen storage applications, *Int. J. Hydrogen Energy*, 2025, **154**, 150299.
23 W. Azeem, M. K. Shahzad, Y. H. Wong and M. B. Tahir, Ab-initio calculations for the study of the hydrogen storage properties of $CsXH_3$ (X = Co, Zn) perovskite-type hydrides, *Int. J. Hydrogen Energy*, 2024, **50**, 305–313.
24 W. Azeem, *et al.*, Computational insights of double perovskite X_2CaCdH_6 (X = Rb and Cs) hydride materials for hydrogen storage applications: a DFT analysis, *Int. J. Hydrogen Energy*, 2024, **79**, 514–524.
25 H. Alkhalidi, S. Isied, A. Almahmoud and A. Obeidat, Theoretical Investigation of Double Perovskite Hydrides X_2CaAlH_6 (X = K, Rb, and Cs) for Hydrogen Storage Applications, 2025, preprint, DOI: 10.2139/ssrn.5134289.
26 M. K. Shahzad, *et al.*, Computational insights of double perovskite Na_2CaCdH_6 hydride alloy for hydrogen storage applications: a DFT investigation, *Sci. Rep.*, 2024, **14**, 1–12.
27 H. Murtaza, *et al.*, The prediction of hydrogen storage capacity and solar water splitting applications of Rb_2AlXH_6 (X = In, Tl) perovskite halides: a DFT study, *J. Phys. Chem. Solids*, 2025, **198**, 112427.
28 H. D. Alkhaldi, Study of physical aspects and hydrogen storage potential of X_2LiBH_6 (X = K, Rb); a DFT investigation, *J. Energy Storage*, 2025, **132**, 117890.

29 A. Ayyaz, *et al.*, Investigation of hydrogen storage and energy harvesting potential of double perovskite hydrides A_2LiCuH_6 (A = Be/Mg/Ca/Sr): a DFT approach, *Int. J. Hydrogen Energy*, 2025, **102**, 1329–1339.
30 Y. A. Kumar and H.-J. Kim, Preparation and electrochemical performance of $NiCo_2O_4$@$NiCo_2O_4$ composite nanoplates for high-performance supercapacitor applications, *New J. Chem.*, 2018, **42**, 19971–19978.
31 S. A. Hira, S. Nagappan, D. Annas, Y. A. Kumar and K. H. Park, NO_2-functionalized metal–organic framework incorporating bimetallic alloy nanoparticles as a sensor for efficient electrochemical detection of dopamine, *Electrochem. Commun.*, 2021, **125**, 107012.
32 A. K. Yedluri and H.-J. Kim, Wearable super-high specific performance supercapacitors using a honeycomb with folded silk-like composite of $NiCo_2O_4$ nanoplates decorated with $NiMoO_4$ honeycombs on nickel foam, *Dalton Trans.*, 2018, **47**, 15545–15554.
33 T. Tang and Y. Tang, First-principles investigations for the structural, optoelectronic and hydrogen storage properties of double perovskite $KNaMg_2F_{6-x}H_x$ and $KNaAe_2H_6$ (Ae = Be, Mg, Ca), *Int. J. Hydrogen Energy*, 2024, **61**, 13–24.
34 P. Blaha, K. Schwarz, P. Sorantin and S. B. Trickey, Full-potential, linearized augmented plane wave programs for crystalline systems, *Comput. Phys. Commun.*, 1990, **59**, 399–415.
35 Ł. Szeleszczuk, K. Mądra-Gackowska and M. Gackowski, High-efficiency thermoelectric performance of X_2YN_2 (X = Zr, Hf; YS, Se) Zintl phases: a first-principles study, *Mater. Chem. Phys.*, 2026, **353**, 132115.
36 T. Bellakhdar, Z. Nabi, B. Bouabdallah, B. Benichou and H. Saci, Ab initio study of structural, electronic, mechanical and optical properties of the tetragonal $Cs_2AgBiBr_6$ halide double perovskite, *Appl. Phys. Mater. Sci. Process.*, 2022, **128**, 155.
37 A. Ayyaz, *et al.*, Lead-Free Double Perovskites Rb_2TlSbX_6 (X = Cl, Br, and I) As an Emerging Aspirant for Solar Cells and Green Energy Applications, *Sol. Energy*, 2024, **279**, 112844.
38 F. Tran and P. Blaha, Accurate band gaps of semiconductors and insulators with a semilocal exchange-correlation potential, *Phys. Rev. Lett.*, 2009, **102**, 226401.
39 S. Mahmud, M. A. U. Z. Atik, M. N. Mostakim, M. Tarekuzzaman and M. Z. Hasan, Investigation of direct small bandgap Cs_2AuInX_6 (X = F/Cl) double perovskites for energy harvesting technology employing DFT, *Comput. Condens. Matter*, 2024, **40**, e00950.
40 S. Mahmud, M. M. Hossain, M. M. Uddin and M. A. Ali, Prediction of X_2AuYZ_6 (X = Cs, Rb; Z = Cl, Br, I) double halide perovskites for photovoltaic and wasted heat management device applications, *J. Phys. Chem. Solids*, 2025, **196**, 112298.
41 M. S. Parves, *et al.*, Structural and optoelectronic study of $MgLiX_3$ (X = Cl, Br, and I) halide perovskites: a DFT approach, *AIP Adv.*, 2024, **14**(10), 105034.
42 M. Tahir, M. Usman, J. U. Rehman and M. B. Tahir, A first-principles study to investigate the physical properties of Sn-based hydride perovskites $XSnH_3$ (X = K, Li) for hydrogen storage application, *Int. J. Hydrogen Energy*, 2024, **50**, 845–853.
43 X. Du, D. He, H. Mei, Y. Zhong and N. Cheng, Insights on electronic structures, elastic features and optical properties of mixed-valence double perovskites $Cs_2Au_2X_6$ (X = F, Cl, Br, I), *Phys. Lett. A*, 2020, **384**, 126169.
44 C. J. Bartel, Review of computational approaches to predict the thermodynamic stability of inorganic solids, *J. Mater. Sci.*, 2022, **57**, 10475–10498.
45 M. Irfan, E. M. Ahmed, S. A. M. Issa and H. M. H. Zakaly, Principles-based investigation of lithium-based halide perovskite X_2LiAlH_6 (X = K, Mn) for hydrogen storage, optoelectronic, and radiation shielding applications, *Int. J. Hydrogen Energy*, 2024, **91**, 775–786.
46 S. Mahmud, M. A. Ali, M. M. Hossain and M. M. Uddin, DFT aided prediction of phase stability, optoelectronic and thermoelectric properties of A_2AuScX_6 (A = Cs, Rb; X = Cl, Br, I) double perovskites for energy harvesting technology, *Vacuum*, 2024, **221**, 112926.
47 Z. Gao, *et al.*, High-throughput screening of promising lead-free inorganic halide double perovskites via first-principles calculations, *Phys. Chem. Chem. Phys.*, 2022, **24**, 3460–3469.
48 G. Surucu, A. Candan, A. Gencer and M. Isik, First-principle investigation for the hydrogen storage properties of $NaXH_3$ (X = Mn, Fe, Co) perovskite type hydrides, *Int. J. Hydrogen Energy*, 2019, **44**, 30218–30225.
49 N. Xu, Y. Chen, S. Chen, S. Li and W. Zhang, First-principles investigation for the hydrogen storage properties of $XTiH_3$ (X = K, Rb, Cs) perovskite type hydrides, *Int. J. Hydrogen Energy*, 2024, **50**, 114–122.
50 N. Al-Zoubi, A. Almahmoud and A. Obeidat, Impact of vanadium and zirconium contents on properties of novel lightweight $Ti_3Zr_yNbV_x$ refractory high-entropy alloys, *Solids*, 2025, **6**(1), 2.
51 C. E. M. Campos, *et al.*, Influence of minor oxidation of the precursor powders to form nanocrystalline CdTe by mechanical alloying, *J. Alloys Compd.*, 2008, **466**, 80–86.
52 M. Born, On the stability of crystal lattices. I, *Math. Proc. Camb. Philos. Soc.*, 1940, **36**, 160–172.
53 Z. J. Wu, *et al.*, Crystal structures and elastic properties of superhard IrN_2 and IrN_3 from first principles, *Phys. Rev. B: Condens. Matter Mater. Phys.*, 2007, **76**, 054115.
54 S. Al, M. Yortanlı and E. Mete, Lithium metal hydrides (Li_2CaH_4 and Li_2SrH_4) for hydrogen storage; mechanical, electronic and optical properties, *Int. J. Hydrogen Energy*, 2020, **45**, 18782–18788.
55 X. Liu and J. Fu, First principle study on electronic structure, elastic properties, and debye temperature of pure and doped $KCaF_3$, *Vacuum*, 2020, **179**, 109504.
56 J. A. Abraham, DFT-focused estimation of mechanical, thermoelectric, and thermodynamic properties of $ACdF_3$ (A = K, Rb, Cs) fluroperovskites, *Int. J. Mod. Phys. B*, 2019, **33**(27), 1950314.
57 S. Al, Mechanical and electronic properties of perovskite hydrides $LiCaH_3$ and $NaCaH_3$ for hydrogen storage applications, *Eur. Phys. J. B*, 2021, **94**, 1–9.

58 W. J. Yin, T. Shi and Y. Yan, Unusual defect physics in $CH_3NH_3PbI_3$ perovskite solar cell absorber, *Appl. Phys. Lett.*, 2014, **104**(6), 063903.
59 M. Archi, O. Bajjou, K. Rahmani and B. Elhadadi, Investigation of structural, phonon, thermodynamic, electronic, and mechanical properties of non-toxic $XZnH_3$ (X = Li, Na, K) perovskites for solid-state hydrogen storage: a DFT and AIMD approach, *J. Energy Storage*, 2025, **112**, 115492.
60 M. Archi, O. Bajjou, K. Rahmani and B. Elhadadi, A comparative ab initio analysis of the stability, electronic, thermodynamic, mechanical, and hydrogen storage properties of $SrZnH_3$ and $SrLiH_3$ perovskite hydrides through DFT and AIMD Approaches, *Int. J. Hydrogen Energy*, 2025, **105**, 759–770.
61 F. Tran and P. Blaha, Accurate band gaps of semiconductors and insulators with a semilocal exchange-correlation potential, *Phys. Rev. Lett.*, 2009, **102**, 226401.
62 K. Mądra-Gackowska, M. Gackowski and Ł. Szeleszczuk, Density functional theory insights into A_2BBiCl_6 (A = Cs, K; B = Ag, Au) halide double perovskites for next-generation photovoltaics, *Phys. B*, 2026, **726**, 418286.
63 Ł. Szeleszczuk, K. Mądra-Gackowska, V. B. Hacholli and M. Gackowski, Designing efficient energy materials: optoelectronic and thermoelectric perspectives of X_2YBiCl_6 (X = Cs, Na; Y = Ag, Au) double perovskites, *J. Phys. Chem. Solids*, 2026, **209**, 113293.
64 S. Maqsood, *et al.*, First-principle investigation of thermoelectric and optoelectronic properties of Rb_2KScI_6 and Cs_2KScI_6 double perovskite for solar cell devices, *J. Mater. Res. Technol.*, 2022, **21**, 841–849.
65 M. Ullah, E. Ahmed, F. Hussain, A. M. Rana and R. Raza, Electrical conductivity enhancement by boron-doping in diamond using first principle calculations, *Appl. Surf. Sci.*, 2015, **334**, 40–44.
66 S. Mahmud, *et al.*, Novel $Cs_2Au^IM^{III}F_6$ (M = As, Sb) double halide perovskites: sunlight and industrial waste heat management device applications, *Phys. Chem. Chem. Phys.*, 2025, **27**, 4686–4703.
67 A.-A. Md, *et al.*, Numerical optimization of $Rb_2AuScBr_6$ and $Rb_2AuScCl_6$-based lead-free perovskite solar cells: device engineering and performance mapping, *RSC Adv.*, 2025, **15**, 45309–45330.
68 S. Mahmud, Md. M. Islam, Md. M. Hossain, Md. M. Uddin and Md. A. Ali, Performance Engineering of Cs_2AuScI_6 Double Halide Perovskite Solar Cell: A DFT and SCAPS-1D Approach to 31.82% Efficiency, *Adv. Theory Simul.*, 2026, **9**, e01693.
69 Ł. Szeleszczuk, K. Mądra-Gackowska and M. Gackowski, From oxide to sulfide: computational design of $NaTaO_{3-x}S_x$ perovskites with tailored electronic and thermal behavior, *Vacuum*, 2026, **248**, 115212.
70 M. K. Shahzad, *et al.*, First principle investigation of tungsten-based cubic oxide perovskite materials for superconducting applications: a DFT study, *J. Phys. Chem. Solids*, 2024, **186**, 111813.
71 S. Hussain, J. U. Rehman, A. Hussain, M. B. Tahir and F. Iqbal, Study of double perovskite materials $RbX_2Y_3O_{10}$ (X = Mg, Ca, Y = Ti, Zr) for photocatalytic applications: a DFT insights, *Int. J. Hydrogen Energy*, 2024, **62**, 739–748.
72 T. Tang and Y. Tang, First-principles investigations for the structural, optoelectronic, and hydrogen storage properties of double perovskite $KNaMg_2F_{6-x}H_x$ and $KNaAe_2H_6$ (Ae = Be, Mg, Ca), *Int. J. Hydrogen Energy*, 2024, **61**, 13–24.
73 Q. Mahmood, T. Ghrib, A. Rached, A. Laref and M. A. Kamran, Probing of mechanical, optical, and thermoelectric characteristics of double perovskites Cs_2GeCl/Br_6 by DFT method, *Mater. Sci. Semicond. Process.*, 2020, **112**, 105009.
74 A. Ayyaz, G. Murtaza, M. Umer, A. Usman and H. H. Raza, Structural, elastic, optoelectronic, and transport properties of Na-based halide double perovskites Na_2CuMX_6 (M = Sb, Bi, and X = Cl, Br) as renewable energy materials: a DFT insight, *J. Mater. Res.*, 2023, **38**, 4609–4624.
75 Y. Zhou, *et al.*, Advances in ionogels for proton-exchange membranes, *Sci. Total Environ.*, 2024, **921**, 171099.
76 P. Y. Yu and M. Cardona, *Fundamentals of Semiconductors*, 2005, DOI: 10.1007/B137661.
77 J. Xie*et al.*, Perovskite solar cells processed by solution nanotechnology, *Advanced Nanomaterials for Solar Cells and Light Emitting Diodes*, Elsevier, 2019, pp. 119–174.
78 H. J. Snaith, Perovskites: The Emergence of a New Era for Low-Cost, High-Efficiency Solar Cells, *J. Phys. Chem. Lett.*, 2013, **4**, 3623–3630.
79 R. M. A. Khalil, *et al.*, DFT-based study of the structural, optoelectronic, mechanical, and magnetic properties of Ti_3AC_2 (A = P, As, Cd) for coating applications, *RSC Adv.*, 2022, **12**, 4395–4407.
80 H. Shinotsuka, H. Yoshikawa and S. Tanuma, First-principles Calculations of Optical Energy Loss Functions for 30 Compound and 5 Elemental Semiconductors, *e-J. Surf. Sci. Nanotechnol.*, 2021, **19**, 70–87.
81 B. Ehrler, *et al.*, Photovoltaics Reaching for the Shockley–Queisser Limit, *ACS Energy Lett.*, 2020, **5**, 3029–3033.
82 M. K. Masood, *et al.*, Physical properties of the $XScH_3$ (X: Ca, and Mg) perovskite hydrides and their hydrogen storage applications, *J. Phys. Chem. Solids*, 2024, **192**, 112098.
83 M. H. Kuo, N. Neykova and I. Stachiv, Overview of the Recent Findings in the Perovskite-Type Structures Used for Solar Cells and Hydrogen Storage, *Energy*, 2024, **17**, 4755.
84 M. Tahir, M. Usman, J. U. Rehman and M. B. Tahir, A first-principles study to investigate the physical properties of Sn-based hydride perovskites $XSnH_3$ (X = K, Li) for hydrogen storage application, *Int. J. Hydrogen Energy*, 2024, **50**, 845–853.
85 R. Zosiamliana, *et al.*, A comprehensive first principles investigation of A_2BH_6 type (A = Li, Na, and K; B = Al, and Si) double perovskite hydrides for high capacity hydrogen storage, *arXiv*, 2025, preprint, arXiv:2507.19810, DOI: 10.48550/arXiv:2507.19810.
86 R. K. Pan, J. G. Yao, R. L. Ji, W. W. Liu and D. F. Yin, First principles study on elastic and electronic properties of bialkali alanates $M_2M'AlH_6$, *Int. J. Hydrogen Energy*, 2018, **43**, 3862–3870.

87 L. G. Anupam, S. Kumar, S. Panwar and S. Diwaker, Ab initio studies of newly proposed zirconium-based novel combinations of hydride perovskites $ZrXH_3$ (X = Zn, Cd) for hydrogen storage applications, *Int. J. Hydrogen Energy*, 2024, **55**, 1465–1475.

88 S. Al, Mechanical and electronic properties of perovskite hydrides $LiCaH_3$ and $NaCaH_3$ for hydrogen storage applications, *Eur. Phys. J. B*, 2021, **94**(9), 182.

89 M. Pozzo and D. Alfè, Dehydrogenation of pure and Ti-doped Na_3AlH_6 surfaces from first principles calculations, *Int. J. Hydrogen Energy*, 2011, **36**, 15632–15641.

90 J. Puszkiel, A. Gasnier, G. Amica and F. Gennari, Tuning $LiBH_4$ for hydrogen storage: Destabilization, additive, and nanoconfinement approaches, *Molecules*, 2019, **25**(1), 163.

91 X. Yang, W. Li, J. Zhang and Q. Hou, Hydrogen storage performance of Mg/MgH_2 and its improvement measures: research progress and trends, *Materials*, 2023, **16**(4), 1587.

92 G. Sandrock, K. Gross and G. Thomas, Effect of Ti-catalyst content on the reversible hydrogen storage properties of the sodium alanates, *J. Alloys Compd.*, 2002, **339**, 299–308.

93 A. Ayyaz, *et al.*, Exploring hydrogen storage potential, thermodynamic, and optoelectronic characteristics of novel double perovskite hydrides Na_2LiXH_6 (X = Al, Sc, and Ga): DFT analysis, *J. Energy Storage*, 2025, **122**, 116650.

94 Q. Dai, T. Y. Tang, Z. Q. Chen, Y. Wang and Y. L. Tang, A DFT study to investigate of K_2LiXH_6 (X = Al, Ga, In) perovskite hydrides for hydrogen storage application, *Int. J. Hydrogen Energy*, 2025, **101**, 295–302.

95 M. K. Shahzad, *et al.*, Computational insights of double perovskite Na_2CaCdH_6 hydride alloy for hydrogen storage applications: a DFT investigation, *Sci. Rep.*, 2024, **14**, 1–12.

96 H. Murtaza, *et al.*, First-Principles Prediction of the Optoelectronic, Mechanical, Thermodynamic and Hydrogen Storage Attributes of Double Perovskite Rb_2NaXH_6 (X = Al, In), *Polym. Mater.*, 2025, **35**, 2877–2888.

97 W. Azeem, *et al.*, Computational insights of double perovskite X_2CaCdH_6 (X = Rb and Cs) hydride materials for hydrogen storage applications: a DFT analysis, *Int. J. Hydrogen Energy*, 2024, **79**, 514–524.

98 N. Al-Zoubi, H. Al-Khalidi, A. Jaradat and A. Obeidat, Investigation of Ba_2XYH_6 (X = Li, Na; Y = V, Nb) double perovskite hydrides for hydrogen storage: a computational approach, *Mater. Chem. Phys.*, 2025, **344**, 131175.

99 A. Fujishima and K. Honda, Electrochemical photolysis of water at a semiconductor electrode, *Nature*, 1972, **238**(5358), 37–38.

100 T. R. Harris-Lee, F. Marken, C. L. Bentley, J. Zhang and A. L. Johnson, A chemist's guide to photoelectrode development for water splitting – the importance of molecular precursor design, *EES Catal.*, 2023, **1**, 832–873.

101 Y. Cai, *First-principles Discovery and Investigation of Novel Materials for Energy Conversion*, 2019.

102 H. H. AbdElAziz, M. Taha, W. M. A. El Rouby, M. H. Khedr and L. Saad, Evaluating the performance of $Cs_2PtI_{6-x}Br_x$ for photovoltaic and photocatalytic applications using first-principles study and SCAPS-1D simulation, *Heliyon*, 2022, **8**, e10808.

103 A. N. Corpus-Mendoza, P. M. Moreno-Romero and H. Hu, Evaluation of Mulliken Electronegativity on $CH_3NH_3PbI_3$ Hybrid Perovskite as a Thought-Provoking Activity, *J. Chem. Educ.*, 2019, **96**, 974–978.

104 F. Sun, *et al.*, Construction of strontium tantalate homo-semiconductor composite photocatalysts with a tunable type II junction structure for overall water splitting, *Catal. Sci. Technol.*, 2018, **8**, 3025–3033.

105 I. Hamideddine, H. Jebari, N. Tahiri, O. El Bounagui and H. Ez-Zahraouy, The investigation of the electronic, optical, and thermoelectric properties of the Ge-based halide perovskite $AGeI_2Br$ (a = K, Rb, Cs) compound for a photovoltaic application: first principles calculations, *Int. J. Energy Res.*, 2022, **46**, 20755–20765.

106 R. G. Pearson, Absolute electronegativity and hardness: application to inorganic chemistry, *Inorg. Chem.*, 1988, **27**, 734–740.

107 K. Maeda, Photocatalytic water splitting using semiconductor particles: history and recent developments, *J. Photochem. Photobiol., C*, 2011, **12**, 237–268.

108 X. Chen, *et al.*, Semiconductor-based photocatalytic hydrogen generation, *Chem. Rev.*, 2010, **110**, 6503–6570.

109 A. J. Bard and M. Anne Fox., Artificial photosynthesis: solar splitting of water to hydrogen and oxygen, *Acc. Chem. Res.*, 1995, **28**, 141–145.

110 T. Hisatomi, J. Kubota and K. Domen, Recent advances in semiconductors for photocatalytic and photoelectrochemical water splitting, *Chem. Soc. Rev.*, 2014, **43**, 7520–7535.

111 A. Fujishima, X. Zhang and D. A. Tryk, TiO_2 photocatalysis and related surface phenomena, *Surf. Sci. Rep.*, 2008, **63**, 515–582.

112 A. V. Zhurenok, D. B. Vasilchenko and E. A. Kozlova, Comprehensive Review on g-C_3N_4-Based Photocatalysts for the Photocatalytic Hydrogen Production under Visible Light, *Int. J. Mol. Sci.*, 2022, **24**, 346.